

Investigation on Elasticity-Based Tissue Characterization of Arterial Wall

Hideyuki Hasegawa^{1,2} and Hiroshi Kanai^{2,1}

1 Graduate School of Biomedical Engineering, Tohoku University

2 Graduate School of Engineering, Tohoku University

E-mail: hasegawa@ecei.tohoku.ac.jp, hkanai@ecei.tohoku.ac.jp



Abstract

Artery-wall motion due to the pulsation of the heart is often measured to evaluate mechanical properties of the arterial wall. Such motion is thought to occur only in the arterial radial direction because the main source of the motion is an increase of blood pressure. However, it has recently been reported that the artery also moves in the longitudinal direction. Therefore, a 2-D motion estimator is required even when the artery is scanned in the longitudinal direction because the arterial wall moves both in the radial (axial) and longitudinal (lateral) directions. Methods based on 2-D correlation of RF echoes are often used to estimate the lateral displacement together with axial displacement. However, these methods require much interpolation of the RF echo or correlation function to achieve a sufficient resolution in the estimation of displacement. To overcome this problem, Jensen *et al.* modulated the ultrasonic field in the lateral direction at a designed spatial frequency to use the lateral phase for the estimation of lateral motion. This method, namely, the lateral modulation method, generates complex signals whose phases change depending on the lateral motion. Therefore, the lateral displacement can be estimated with a good resolution without interpolation, although special beamformers are required. The present paper describes a method that can be applied to ultrasonic echoes obtained by a conventional beamformer to estimate lateral displacements using the phases of lateral fluctuations of ultrasonic echoes. In the proposed method, complex signals were generated by the Hilbert transform, and the phase shift was estimated by correlation-based estimators. The proposed method was validated using a cylindrical phantom mimicking an artery. The error in the lateral displacement estimated by the proposed method was 13.5% of the true displacement of 0.5 mm with a kernel size used for calculating the correlation function of 0.6 mm in the lateral direction, which was slightly smaller than the width at -20 dB of the maximum lateral ultrasonic field (about 0.8 mm).

1. Introduction

Noninvasive measurement of mechanical properties of the arterial wall, such as elasticity, is useful for diagnosing atherosclerosis because there are significant

differences between the elastic moduli of normal arterial walls and those affected by atherosclerosis [1-3]. In particular, mechanical properties of plaque are important because the rupture of plaque may cause acute myocardial infarction and cerebral infarction [4-6]. Magnetic resonance imaging (MRI) and intravascular ultrasound (IVUS) are promising technologies for directly imaging plaque morphology [7,8]. On the other hand, the dynamic change of artery diameter due to the pulsation of the heart can be measured noninvasively by the previous method with ultrasound [9-13]. Some parameters related to artery-wall elasticity can be obtained by the measured change in diameter of the artery [14-16]. However, in the derivation of these parameters, the artery is assumed to be a cylindrical shell with a uniform wall thickness and, thus, the elasticity of atherosclerotic plaque cannot be evaluated.

For measurement of the mechanical properties of the arterial wall, including the case with atherosclerotic plaque, we previously developed a method, namely, the *phased tracking method*, for measuring small vibrations in the heart wall or arterial wall with transcutaneous ultrasound [17,18]. For some years, we have been measuring the displacement and small change in thickness of the arterial wall caused by the heartbeat using this method [19-22]. In our *phased tracking method*, a set of two points is assigned along an ultrasonic beam, and the change in thickness of the layer between these two points is estimated. Furthermore, by sliding the position of the layer along the ultrasonic beam by intervals of the sampled points, the spatial distribution of changes in thickness along the ultrasonic beam can be obtained.

In the above-mentioned methods including our method, the radial motion of the arterial wall, such as changes in diameter [9-13] and radial strain [19-22], are measured because it is considered that the source of the artery-wall motion is the change in internal pressure (blood pressure) and that there is no longitudinal motion. However, Cinthio *et al.* showed that the artery also moves in the longitudinal direction [23]. Therefore, a 2-D motion estimator is required to estimate both the axial (radial) and lateral (longitudinal) displacements, even when an artery is scanned in the longitudinal direction.

de Korte *et al.* introduced a motion estimator based on the correlation between RF echoes to measure the 2-D displacement of the arterial wall in the cross-sectional scan [24]. Such a motion estimator based on

correlation between RF echoes had previously been developed and thoroughly investigated in the field of tissue elasticity imaging [25-28], results indicating that it accurately estimates the 2-D displacement. However, much interpolation is required to realize an accurate estimation.

Jensen *et al.* introduced a method, namely, the lateral modulation method, in which the ultrasonic field is modulated in the lateral direction at a designed spatial frequency to realize a lateral displacement estimation using the lateral phase induced by the modulated field [29]. This method generates complex signals whose phases change depending on the lateral displacement and, therefore, the lateral displacement can be estimated with a good resolution because the phase change can be directly converted into the lateral displacement. However, this method requires special beamformers that are not available in conventional equipment.

To overcome this problem, Chen *et al.* recently proposed a method to estimate lateral displacements using the lateral phases of ultrasonic echoes obtained by conventional beamformers [30]. The accurate estimation of lateral displacements would be very useful, particularly when it could be done based on conventional beamformers. The present paper describes a method, which also uses the lateral phases of echoes obtained by conventional beamformers, for estimation of lateral displacements of arterial walls [31]. In the proposed method, complex signals are generated by the Hilbert transform, and the phase shift due to the lateral motion is estimated by a correlation-based estimator. The proposed method was validated using a cylindrical phantom mimicking an artery and compared with the lateral modulation method.

2. Materials and Methods

2.1. Difficulties Encountered in Estimation of Lateral Motion Using Phases of Ultrasonic Echoes

This section describes the fundamental theory of ultrasonic fields to show why it is difficult to use the phase information of ultrasonic echoes for estimation of lateral motion.

When the ultrasonic field is focused at a depth of interest z using a linear array probe, a point spread function (PSF) $h(x)$ is created as illustrated in Fig. 1, where only its profile in the lateral direction x at depth z is considered. By defining the spatial distribution of the amplitude reflection coefficient of an object in the n -th frame as $r(x; n)$, the amplitude $s(x; n)$ of an echo at depth z obtained by an ultrasonic beam focused at the point of interest (x, z) is expressed as follows:

$$\begin{aligned} s(x; n) &= \int_{-\infty}^{\infty} h(\xi) \cdot r(\xi - x; n) d\xi \\ &= \int_{-\infty}^{\infty} h(\xi) \cdot r(x - \xi; n) d\xi \\ &= h(x) * r(x; n), \end{aligned} \quad (1)$$

where $*$ denotes convolution.

Let $u_x(n)$ be the lateral displacement of the object between the n -th and $(n + 1)$ -th frames. Reflection coefficient $r(x; n + 1)$ in the $(n + 1)$ -th frame is expressed by $r(x; n + 1) = r(x - u_x(n); n)$, where it can be assumed that there is only the lateral motion when the axial motion is compensated by an axial motion estimator (in this study, the method proposed in [32] was used). In addition, it was assumed that there is no distortion in $r(x; n)$ between the n th and $(n + 1)$ -th frames. Under such conditions, the amplitude $s(x; n + 1)$ is given by

$$\begin{aligned} s(x; n + 1) &= h(x) * r(x; n + 1) \\ &= h(x) * r(x - u_x(n); n). \end{aligned} \quad (2)$$

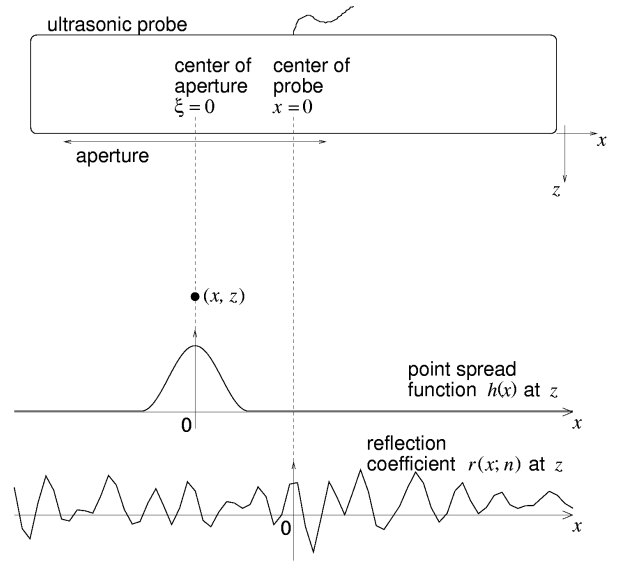


Fig. 1. Geometry for measurement.

In the lateral modulation method proposed by Jensen *et al.* [29], 2 point spread functions, $h_r(x)$ and $h_i(x)$, which oscillate at the same spatial frequency, f_{x0} , but with a phase difference of 90 degrees, are produced to create a complex signal $g(x; n)$, whose phase changes depending on the lateral displacement of the object. Based on the relationship in (1), $g(x; n)$ can be considered to be the complex version of $s(x; n)$. In this case, the 2 point spread functions $h_r(x)$ and $h_i(x)$ are approximately expressed by $\cos(2\pi f_{x0}x)$ and $-\sin(2\pi f_{x0}x)$, respectively. Therefore, complex signal $g(x; n)$ can be obtained based on (1) as follows:

$$\begin{aligned} g(x; n) &= \int_{-\infty}^{\infty} r(x - \xi; n) \cdot (h_r(\xi) + jh_i(\xi)) d\xi \\ &= \int_{-\infty}^{\infty} r(x - \xi; n) \cdot \exp(-j2\pi f_{x0}\xi) d\xi. \end{aligned} \quad (3)$$

As can be seen in (3), the complex signal $g(x; n)$ obtained by the lateral modulation method is the Fourier coefficient $R(f_{x0}; n)$ of reflection coefficient $r(x; n)$ at spatial frequency f_{x0} . Therefore, $g(x; n + 1)$ in the $(n + 1)$ -th frame can be expressed by $g(x; n + 1) = g(x;$

$n) \cdot \exp\{-2\pi f_{x0} u_x(n)\}$. Under such condition, the lateral displacement $u_x(n)$ can be estimated by the phase shift $-2\pi f_{x0} u_x(n)$ from $g(x; n)$ to $g(x; n + 1)$ using the conventional correlation technique because the spatial modulation frequency f_{x0} can be appropriately obtained by designing the point spread functions $h_r(x)$, and $h_i(x)$.

In the present study, the Hilbert transform was applied to RF echoes obtained by conventional beamforming to use the lateral phase. Complex spectrum $S(f_x; n)$ of $s(x; n)$ of (1) is expressed by $H(f_x; n)$ and $R(f_x; n)$ of the point spread function $h(x)$ and reflection coefficient $r(x; n)$ at spatial frequency f_x as $S(f_x; n) = H(f_x) \cdot R(f_x; n)$. Complex spectra $H(f_x)$ and $R(f_x; n)$ are described as follows:

$$H(f_x) = \int_{-\infty}^{\infty} h(\xi) \cdot e^{-j2\pi f_x \xi} d\xi \quad (4)$$

$$R(f_x; n) = \int_{-\infty}^{\infty} r(\xi; n) \cdot e^{-j2\pi f_x \xi} d\xi \quad (5)$$

Analytic signal $y(x; n)$ of $s(x; n)$ is obtained by the inverse Fourier transform of $S(f_x; n)$ in the range of positive spatial frequencies as follows:

$$\begin{aligned} y(x; n) &= \int_0^{\infty} H(f_x) \cdot R(f_x; n) \cdot e^{2\pi f_x x} df_x \\ &= \int_{-\infty}^{\infty} H'(f_x) \cdot R'(f_x; n) \cdot e^{2\pi f_x x} df_x \\ &= h'(x) * r'(x; n), \end{aligned} \quad (6)$$

where

$$H'(f_x) = \begin{cases} H_x(f_x) & (f_x \geq 0), \\ 0 & (f_x < 0), \end{cases} \quad (7)$$

$$R'(f_x; n) = \begin{cases} R(f_x; n) & (f_x \geq 0), \\ 0 & (f_x < 0), \end{cases} \quad (8)$$

$$h'(x) = \int_{-\infty}^{\infty} H'(f_x) \cdot e^{j2\pi f_x x} df_x \quad (9)$$

$$\Leftrightarrow H'(f_x) = \int_{-\infty}^{\infty} h(\xi) \cdot e^{-2\pi f_x \xi} d\xi,$$

$$r'(x; n) = \int_{-\infty}^{\infty} R'(f_x; n) \cdot e^{j2\pi f_x x} df_x \quad (10)$$

$$\Leftrightarrow R'(f_x; n) = \int_{-\infty}^{\infty} r(\xi; n) \cdot e^{-j2\pi f_x \xi} d\xi.$$

In the integration of (6), in a strict sense, the direct current component (at $f_x = 0$) should be multiplied by 0.5. However, in this study, the direct current component in the measured signal $s(x; n)$ was removed before applying the Fourier transform to $s(x; n)$. In this case, the Hilbert transform can be expressed by (6).

Similarly, the analytic signal $y(x; n + 1)$ of $s(x; n + 1)$ in the $(n + 1)$ -th frame is expressed as follows:

$$\begin{aligned} y(x; n + 1) &= \int_{-\infty}^{\infty} H'(f_x) \cdot R'(f_x; n) \cdot D(f_x) \cdot e^{-j2\pi f_x u_x(n)} \\ &\quad \cdot e^{j2\pi f_x x} df_x \\ &= h'(x) * r'(x; n) * \int_0^{\infty} e^{j2\pi f_x (x - u_x(n))} df_x. \end{aligned} \quad (11)$$

In actual measurements, $s(x; n)$ is sampled at the interval of scan lines Δx , and the sampled version of $s(x; n)$ is denoted by $s(m\Delta x; n) \equiv s(m; n)$ ($m = -M/2, -M/2 + 1, \dots, -2, -1, 0, 1, 2, \dots, M/2$), where $M + 1$ is the number of scan lines (lateral length of the scanned region $L = M \cdot \Delta x$). In such a discrete system, (6) and (11) are denoted in the digital system as follows:

$$y(m; n) = h'(m) * r'(m; n), \quad (12)$$

$$\begin{aligned} y(m; n + 1) &= h'(m) * r'(m; n) \\ &\quad * \frac{1 - e^{j(2\pi/M)(M/2+1)(m - u_x(n)/\Delta x)}}{1 - e^{j(2\pi/M)(m - u_x(n)/\Delta x)}}, \end{aligned} \quad (13)$$

where (12) and (13) are obtained from (6) and (11), respectively, by replacing the integration, spatial frequency f_x , and lateral spatial position x by the summation, $k / (M \cdot \Delta x)$ (discrete spatial frequency), and $m\Delta x$ (discrete spatial position), respectively. As shown in (12) and (13), the phase shift from $y(m; n)$ to $y(m; n + 1)$ actually depends on the lateral displacement $u_x(n)$ of the object between the n -th and $(n + 1)$ -th frames. The phase shift of complex signal $g(x; n)$ of (3) obtained by the lateral modulation method is simply related to lateral displacement $u_x(n)$ such as $g^*(x; n) \cdot g(x; n + 1) = |g(x; n)|^2 \cdot \exp\{j2\pi f_{x0} u_x(n)\}$, where $*$ denotes complex conjugate. However, it is difficult to relate the phase shift from $y(m; n)$ to $y(m; n + 1)$ to the lateral displacement $u_x(n)$ because $h(x)$ cannot be assumed to be a sinusoidal wave fluctuating at a known spatial frequency of f_{x0} when a conventional beamformer is used. This is a major difficulty for utilization of the lateral phase with conventional beamformers. In the present study, a new method was introduced to overcome this problem.

2.2. Principle of Lateral Displacement Estimation Using the Lateral Phase

Let us define the complex correlation function $\gamma(\Delta m; m; n)$ between $y(m; n)$ of (12) and $y(m; n + 1)$ of (13) at lateral lag $\Delta m \cdot \Delta x$ as

$$\gamma(\Delta m; m; n) = \sum_{k=-M_c}^{M_c} y^*(M + k; n) \cdot y(m + \Delta m + k; n + 1), \quad (14)$$

where M_c determines the number of sampled points used for calculating the correlation function.

The phase shift $\Delta\theta(m; n)$ from $y(m; n)$ to $y(m; n + 1)$ induced by lateral displacement $u_x(n)$ between the n -th and $(n + 1)$ -th frames can be obtained by setting lateral lag Δm at 0 (conventional correlation technique [33]) as follows:

$$\begin{aligned} \Delta\theta(m; n) &= \angle \gamma(\Delta m; m; n) \Big|_{\Delta m \rightarrow 0} \\ &= \angle \gamma(0; m; n). \end{aligned} \quad (15)$$

In this study, as illustrated in Fig. 2, it was assumed that there is a linear relationship between the lateral

displacement $u_x(n)$ and the change in the lateral phase $\Delta\theta(m; n)$, as expressed by

$$\begin{aligned} u_x(n) &= a(n) \cdot \Delta\theta(m; n) \\ &= a(n) \cdot \angle \gamma(0; m; n), \end{aligned} \quad (16)$$

where $a(n)$ is a constant (corresponding to the slope of the linear relationship), which linearly relates the phase shift to the lateral displacement.

When Δm is set at 1, it can be considered that $y(m; n + 1)$ of (13) is artificially displaced by Δx (= an interval of scan line) relative to $y(m; n)$ of (12). Therefore, the following relationship holds:

$$u_x(n) + \Delta x = a(n) \cdot \angle \gamma(1; m; n). \quad (17)$$

By solving simultaneous equations consisting of (16) and (17), slope $a(n)$ and lateral displacement $u_x(n)$ are estimated as follows:

$$\begin{aligned} \hat{a}_{(\Delta m_1, \Delta m_2)}(n) \Big|_{\Delta m_1 \rightarrow 0, \Delta m_2 \rightarrow 1} &= \frac{\Delta x}{\angle \gamma(1; m; n) - \angle \gamma(0; m; n)} \quad (18) \\ &= \frac{\Delta x}{\angle (\gamma^*(0; m; n) \cdot \gamma(1; m; n))}, \end{aligned}$$

$$\hat{u}_{x, (\Delta m_1, \Delta m_2)}(n) \Big|_{\Delta m_1 \rightarrow 0, \Delta m_2 \rightarrow 1} = \frac{\Delta x}{\angle (\gamma^*(0; m; n) \cdot \gamma(1; m; n))} \cdot \angle \gamma(0; m; n), \quad (19)$$

where $\hat{a}_{(\Delta m_1, \Delta m_2)}(n)$ and $\hat{u}_{x, (\Delta m_1, \Delta m_2)}(n)$ are the slope and the lateral displacement, respectively, which are estimated by correlation functions at lateral lags from Δm_1 to Δm_2 .

Although more computation is required, other correlation functions at different lateral lags can be used for displacement estimation. As in (17), the following relationship holds:

$$u_x(n) + \Delta m \Delta x = a(n) \angle \gamma(\Delta m; m; n), \quad (20)$$

where it should be noted that $\Delta m \Delta x$ is an artificial displacement.

Using more than 2 correlation functions, lateral displacement $u_x(n)$ of a target can be estimated by the least-squares method. To do that, let us consider the relationship that is obtained by subtracting (16) from (20) as follows:

$$\begin{aligned} \Delta m \Delta x &= a(n) \{ \angle \gamma(\Delta m; m; n) - \angle \gamma(0; m; n) \} \\ &\equiv a(n) \angle \gamma'(\Delta m; m; n), \end{aligned} \quad (21)$$

where $\angle \gamma'(\Delta m; m; n) = \angle \gamma(\Delta m; m; n) - \angle \gamma(0; m; n)$.

By considering the left and right sides of (21) to be the actual and model lateral displacements, respectively, the mean squared difference $\alpha(n)$ between the actual and model displacements is expressed as follows:

$$\begin{aligned} \alpha(n) &= \sum_{\Delta m = \Delta m_1}^{\Delta m_2} \{ \Delta m \Delta x - a(n) \angle \gamma'(\Delta m; m; n) \}^2 \\ &= \sum_{\Delta m = \Delta m_1}^{\Delta m_2} \left[\Delta m^2 \Delta x^2 - 2 \Delta m \Delta x \cdot a(n) \angle \gamma'(\Delta m; m; n) \right. \\ &\quad \left. + a^2(n) \{ \angle \gamma'(\Delta m; m; n) \}^2 \right]. \end{aligned} \quad (22)$$

To determine $\hat{a}_{(\Delta m_1, \Delta m_2)}(n)$ which minimizes the mean squared difference $\alpha(n)$, the partial derivative of (22) with respect to $a(n)$ is set to be zero:

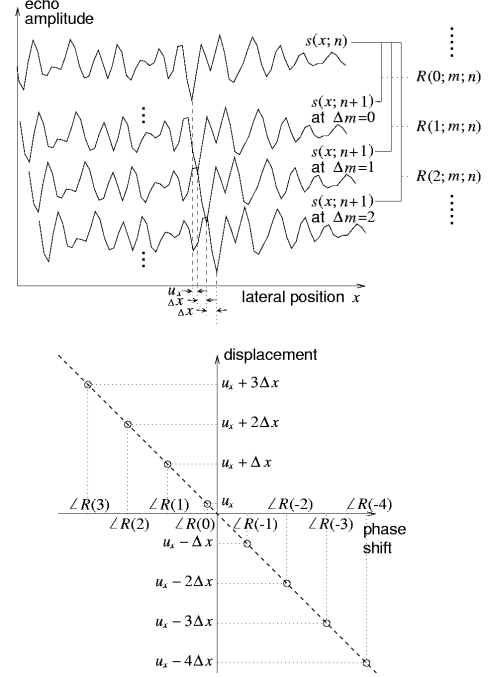


Fig. 2. Assumed relationship between phase shift and lateral displacement. Complex correlation function $\gamma(\Delta m; m; n)$ is shown by $\gamma(\Delta m)$.

$$\begin{aligned} \frac{\partial \alpha}{\partial a} &= -2 \Delta x \sum_{\Delta m = \Delta m_1}^{\Delta m_2} \Delta m \angle \gamma'(\Delta m; m; n) \\ &\quad + 2 a(n) \sum_{\Delta m = \Delta m_1}^{\Delta m_2} \{ \angle \gamma'(\Delta m; m; n) \}^2 \\ &= 0. \end{aligned} \quad (23)$$

By solving (23), $\hat{a}_{(\Delta m_1, \Delta m_2)}(n)$ is obtained as follows:

$$\begin{aligned} \hat{a}_{(\Delta m_1, \Delta m_2)}(n) &= \frac{\Delta x \sum_{\Delta m = \Delta m_1}^{\Delta m_2} \Delta m \angle \gamma'(\Delta m; m; n)}{\sum_{\Delta m = \Delta m_1}^{\Delta m_2} \{ \angle \gamma'(\Delta m; m; n) \}^2} \quad (24) \\ &= \frac{\Delta x \sum_{\Delta m = \Delta m_1}^{\Delta m_2} \Delta m \{ \angle \gamma(\Delta m; m; n) - \angle \gamma(0; m; n) \}}{\sum_{\Delta m = \Delta m_1}^{\Delta m_2} \{ \angle \gamma(\Delta m; m; n) - \angle \gamma(0; m; n) \}^2}. \end{aligned}$$

By substituting (24) into (16), lateral displacement $u_x(n)$ is estimated as follows:

$$\hat{u}_{x,(\Delta m_1, \Delta m_2)}(n) = \frac{\Delta x \sum_{\Delta m = \Delta m_1}^{\Delta m_2} \Delta m \{ \angle \gamma(\Delta m; m; n) - \angle \gamma(0; m; n) \}}{\sum_{\Delta m = \Delta m_1}^{\Delta m_2} \{ \angle \gamma(\Delta m; m; n) - \angle \gamma(0; m; n) \}^2} \cdot \angle \gamma(0; m; n). \quad (25)$$

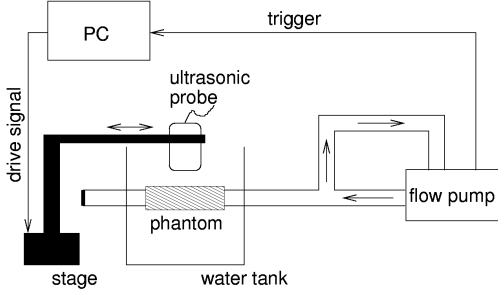


Fig. 3. Schematic of measurement system.

In a subsequent section describing experiments using a phantom, accuracies in estimation of lateral displacements achieved by the 2 estimators, *i.e.*, the computationally efficient version given by (19) and the estimator given by (25) consisting of 3 correlation functions at lags $\{\Delta m\}$ of -1, 0, and 1 ($\Delta m_1 = -1$, $\Delta m_2 = 1$), are compared.

2.3. Experimental System

In this study, a cylindrical phantom (inner diameter: 8 mm; external diameter: 10 mm) made from silicone rubber (elastic modulus: 750 kPa) containing 5% carbon powder (by weight) was measured in the experimental system illustrated in Fig. 3. The radial motion (= axial motion) of the phantom was induced by changing the internal pressure using a flow pump (pulse pressure: about 60 mmHg, theoretical resulting radial strain: about 4%). The longitudinal motion (= lateral motion) was simulated by moving a ultrasonic probe using an automatic stage. The maximum lateral displacements were controlled to be 0.1, 0.25, and 0.5 mm by the automatic stage. The stage was triggered by a signal from the flow pump, which shows the beginning of ejection.

In ultrasonic measurements for the method proposed in this study, RF echoes from the phantom were acquired at a frame rate of 286 Hz with a 10-MHz linear array probe (UST-5545, Aloka, Tokyo, Japan) equipped with conventional ultrasonic diagnostic equipment (SSD-6500, Aloka, Tokyo, Japan). The phantom was scanned in the longitudinal direction at intervals Δx of 0.15 mm (46 scan lines), and RF echoes were sampled at 40 MHz at a 16-bit resolution.

For the lateral modulation method, a scanner (its front end is same as that of α -10 [Aloka, Tokyo, Japan]), which was modified so that RF echoes

received by each array element could be acquired (frame rate: 289 Hz), was employed together with a 10-MHz linear array probe (UST-5545, Aloka, Tokyo, Japan) [34]. With this system, plane waves were transmitted and the receive beamforming was performed with the apodization and delay factors shown in Fig. 4 [29]. Figures 5(a) and 5(b) show a beamformed RF echo from a fine wire (diameter: 16 μ m) placed about 20 mm away from the ultrasonic probe, and Fig. 5(c) shows the spectrum of the echo signal shown in Fig. 5(a) obtained by the 2-D Fourier transform. There were 72 scan lines at lateral intervals Δx of 0.2 mm, and the lateral modulation frequency f_{x0} was set at 0.89 mm^{-1} .

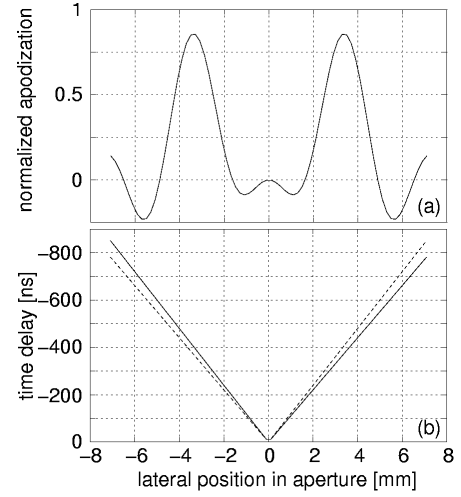


Fig. 4. (a) Amplitude apodization and (b) time delay (for in-phase [solid line] and quadrature [dashed line] beamformers) values for creating the lateral modulation during receive beamforming.

3. Results of Experiments Using a Phantom

3.1. Estimation of Lateral Displacements by the Proposed Method

Fig. 6 shows the procedure to obtain analytic signals $\{y(m; n)\}$. Fig. 6(a) shows RF echoes from the phantom that was scanned in the longitudinal direction using the linear array probe with a conventional beamformer. Envelopes $\{s^2(m; n)\}$ of the RF echoes were detected as shown in Fig. 6(c). The direct current component contained in the envelope signal $s^2(m; n)$ has no phase information and, therefore, it was removed. In this study, the envelope signal without bias was used as echo amplitude $s(m; n)$, which is given by

$$s(m; n) = s^2(m; n) - E_m[s^2(m; n)], \quad (26)$$

where $E[\cdot]$ denotes the averaging operation with respect to lateral position $m \cdot \Delta x$. The Hilbert transform with a Tukey window shown in Fig. 6(b) was then applied to $s(m; n)$ to obtain the analytic signal $y(m; n)$. The real and imaginary parts of analytic signal $y(m; n)$ were obtained as shown in Figs. 6(e) and 6(f).

The method proposed in Section II-B was applied to analytic signal $y(m; n)$ to estimate lateral displacement $u_x(n)$. Twenty points of interest were assigned in the posterior wall at axial intervals of 50 μm along each scan line, and lateral displacements $\{u_x(n)\}$ of these points were estimated. In Figs. 7(1) and 7(2), plots and vertical bars show means and standard deviations of the maximum lateral displacements $\{\hat{u}_{x,(01),\text{max}}(n)\}$ and $\{\hat{u}_{x,(-11),\text{max}}(n)\}$ along each scan line estimated by the estimators given by (19) and (25), respectively, with 4 different sizes of kernels used for calculating correlation function $\gamma(\Delta m; m; n)$ defined by (14). The dashed lines in Fig. 7 show the actual assigned maximum lateral displacements. In calculation of the correlation function, 2-D kernels were used, the axial size of the kernel being fixed to be the optimum value (0.5 μs) determined in [32], and the lateral size of a kernel being changed. In Figs. 7(b), 7(c), 7(d), and 7(e), the lateral sizes of kernels were set at 0.6 mm ($M_c = 2$), 1.2 mm ($M_c = 4$), 2.4 mm ($M_c = 8$), and 3.6 mm ($M_c = 12$), respectively. As shown in Fig. 7, standard deviations were reduced by the estimator consisting of 3 correlation functions given by (25).

Fig. 8 shows rms errors of the estimated lateral displacements obtained by the estimator given by (19) from the actual displacement, where the errors were evaluated from all the estimates except for those obtained at 10 scan lines at each edge of the scanned region because the estimates at these scan lines were influenced by the shape of the Tukey window (not flat). As shown in Fig. 8, the errors were reduced by increasing the size of the correlation kernel, and similar errors resulted from the kernel sizes greater or equal to 2.5 mm.

3.2 Comparison with Results Obtained by the Lateral Modulation Method

Fig. 9(a) shows RF echoes from the phantom obtained by the lateral modulation method (in-phase beamformer), and Fig. 9(b) shows the lateral profiles of RF echoes at a depth indicated by the arrow in Fig. 9(a) obtained by in-phase and quadrature beamformers. As in the displacement estimation by the proposed method, changes in the phases of complex signals $\{g(x; n)\}$ obtained by in-phase and quadrature beamformers were estimated by the correlation technique described in [29] to obtain lateral displacements $\{u_x(n)\}$ at 20 points of interest assigned along each scan line at axial intervals of 50 μm .

As in Section III-A, the use of different lateral sizes of kernels used for calculation of correlation functions was examined. Lateral displacements estimated by applying the motion estimator in [29] to complex signals $\{g(x; n)\}$ obtained by the lateral modulation method are shown in Fig. 10(1). In Figs. 10(1-a), (1-b), (1-c), and (1-d), lateral displacements $\{u_x(n)\}$ were estimated using kernel sizes of 0.6 mm ($M_c = 2$), 1.2 mm ($M_c = 4$), 2.4 mm ($M_c = 8$), and 3.6 mm ($M_c = 12$), respectively. As in Fig. 10(1), lateral displacements obtained by applying the proposed motion estimator to

$\{g(x; n)\}$ are shown in Fig. 10(2) for different correlation kernel sizes. There were no improvements by using the proposed motion estimator together with the lateral modulation method. As shown in Fig. 11, rms errors of the lateral displacements obtained by the motion estimator in [29] were calculated from all the estimates shown in Fig. 10(1).

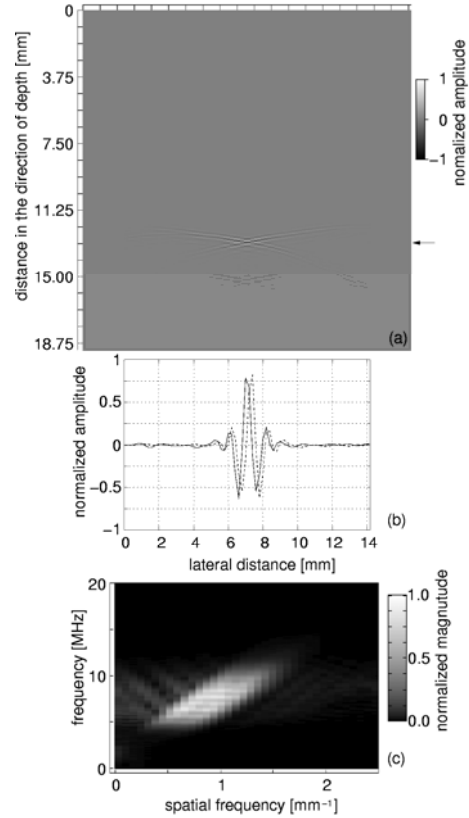


Fig. 5. Radio frequency echo from a fine wire obtained by the lateral modulation method. (a) Radio frequency echo $\text{Re}\{g(x; n)\}$ obtained by inphase receive beamforming, where $\text{Re}\{\cdot\}$ means the real part. (b) Lateral profiles at a depth indicated by the arrow in (a) obtained by in-phase and quadrature receive beamforming. (c) Magnitude of spectrum of the echo signal $\text{Re}\{g(x; n)\}$ shown in (a) obtained by the 2-D Fourier transform.

5. Discussion

In this study, lateral displacements were estimated using the phases of complex signals generated by the Hilbert transform applied to ultrasonic echoes obtained by a conventional beamformer. The phase shift due to the lateral displacement was estimated by the conventional correlation technique, and a larger correlation kernel size in the lateral direction was found to achieve better accuracy. Errors in the estimated lateral displacements were reduced by increasing the kernel size, and similar errors were obtained with kernel sizes greater or equal to 2.5 mm, which roughly corresponds to 3 times the width at -20 dB of the maximum lateral ultrasonic field (about 0.8 mm). In a previous study, the estimation of axial

displacements, the optimal kernel size in the axial direction corresponded to a pulse duration defined by the width at -20 dB of the envelope of an ultrasonic pulse (about 0.4 mm) [32]. In the axial displacement estimation, a smaller kernel relative to the point spread function (0.4 mm) yielded good estimates because there were 2 to 3 oscillations during pulse duration. On the other hand, there was no oscillation in the lateral direction (or more exactly, one oscillation because there was a peak in the lateral profile of the ultrasonic field). Therefore, a kernel size of about 3 times the point spread function was required to minimize the error.

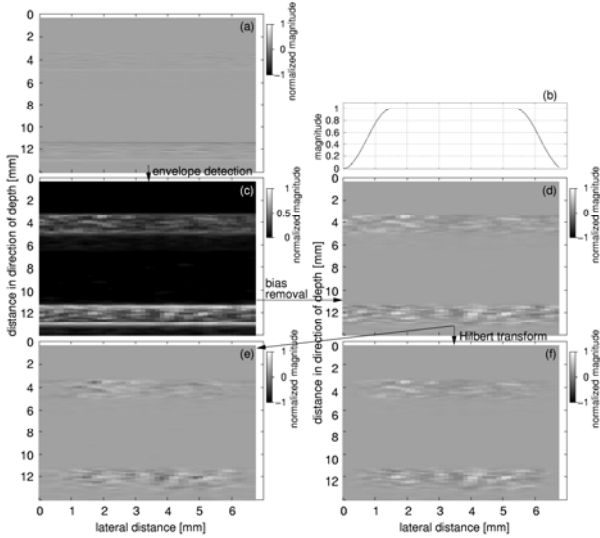


Fig. 6. (a) Radio frequency echoes from the phantom. (b) Tukey window used for frequency analysis of envelope signals of RF echoes. (c) Envelope signals of RF echoes. (d) Envelope signals after bias removal. (e) Imaginary and (f) real part of analytic signals $\{y(x; n)\}$.

To estimate the artery-wall motion using the phases of ultrasonic echoes, it is necessary to avoid the aliasing effect. Therefore, the frame rate f_{FR} should be kept as high as possible. In general, motion of the arterial wall in the radial direction is larger than that in the longitudinal direction, and the oscillation frequency in the axial direction (= radial direction) is higher than that in the lateral direction (= longitudinal direction). Therefore, the aliasing limit for the radial motion (= axial motion) should be considered.

Basically, using the change in the axial phase $\Delta\phi$, the axial velocity v_a is estimated as follows [33], [35]:

$$v_a = \frac{c_0 \Delta\phi}{4\pi f_0} f_{FR}, \quad (27)$$

where c_0 and f_0 are the speed of sound and the center frequency of ultrasound, respectively. In addition, a typical maximal velocity of the carotid arterial wall in the radial direction is about 10 mm/s. The frame rate required for the measurement of the axial motion at 10 mm/s is obtained by substituting $v_a = 10$ mm/s, $\Delta\phi = \pi$ rad, $c_0 = 1500$ m/s, and $f_0 = 10$ MHz into (27) as

follows: $f_{FR} = 4 \times (10 \times 10^{-3}) \times (10 \times 10^6) / 1500 \approx 267$ Hz. To achieve a frame rate higher than 267 Hz at a fixed pulse repetition frequency of 13156 Hz, the number of scan lines was reduced to 46 (this is the lowest available number of scan lines of the employed ultrasonic equipment).

As can be seen in Fig. 8, there is a trade-off between the accuracy and the kernel size (spatial resolution). When we want to estimate the global motion of an object, a large kernel can be used for higher accuracy. On the other hand, it is necessary to use a smaller kernel to obtain the spatial distribution of lateral displacement, although the accuracy will be degraded. Therefore, the method should be optimized depending on the purposes, for example, a greater number of correlation functions in an estimator would reduce standard deviations, as shown in Fig. 7, at the expense of computational efficiency. In addition, further improvements would be required to achieve better accuracy with a smaller kernel. In this study, a linear relationship between the lateral displacement and the change in the phase of the complex signal obtained by the Hilbert transform was assumed. Fig. 12(a) shows a B-mode image of a fine wire (same as that in Fig. 5), and Fig. 12(b) shows a lateral profile of envelopes of RF echoes at a depth indicated by the arrow in Fig. 12(a). By applying the Fourier transform to the lateral profile shown in Fig. 12(b), a power spectrum, which is shown by the solid line in Fig. 12(c), was obtained. As shown by the solid line in Fig. 12(c), in general, the direct current component is largest (central spatial frequency is zero). Therefore, it is difficult to use the lateral phase with conventional beamformers. The dashed line in Fig. 12(c) shows a power spectrum obtained by applying the Fourier transform to the lateral profile after removing the direct current component based on (26). In this case, the power spectrum is largest at a certain spatial frequency ($\neq 0$), and it can be considered that the lateral profile is fluctuating at the central spatial frequency ($\neq 0$), as in the lateral modulation method. Therefore, a linear relationship was assumed in the present paper. In addition, correlation functions in a range from -1 to 1, which corresponded to a range from -150 μ m to 150 μ m in the lateral direction were used for estimation of lateral displacements. This region is much smaller than the size of the width at -20 dB of the maximum lateral ultrasonic field. Therefore, the assumption of the linear relationship between the change in the lateral phase and the lateral displacement in such small range was considered to be appropriate, even when the overall relationship was not perfectly linear. To use a greater number of correlation functions, identification of a better function describing this relationship would be required.

In the present study, although it was assumed that there was no deformation, the proposed method could estimate the lateral displacements of a phantom under a specific degree of deformation. However, a method, in which the distortion of $r(x; n)$ due to deformation of an object is taken into account, should be developed to

improve the accuracy, and such method should be validated under the existence of various degrees of deformation.

In the present study, the results obtained by the proposed method were compared with those obtained by the lateral modulation method. The results obtained by the lateral modulation method with the motion estimator described in [29] were worse than those obtained by the proposed method, and the combination of the lateral modulation method with the motion estimator proposed in the present paper did not achieve any improvements. It could be considered from these results that some optimization might be necessary to obtain correctly modulated fields. Therefore, it cannot be concluded at present that the proposed method is better than the lateral modulation method. Nevertheless, the proposed method would be useful because it can be applied to the ultrasonic echoes obtained by conventional beamformers.

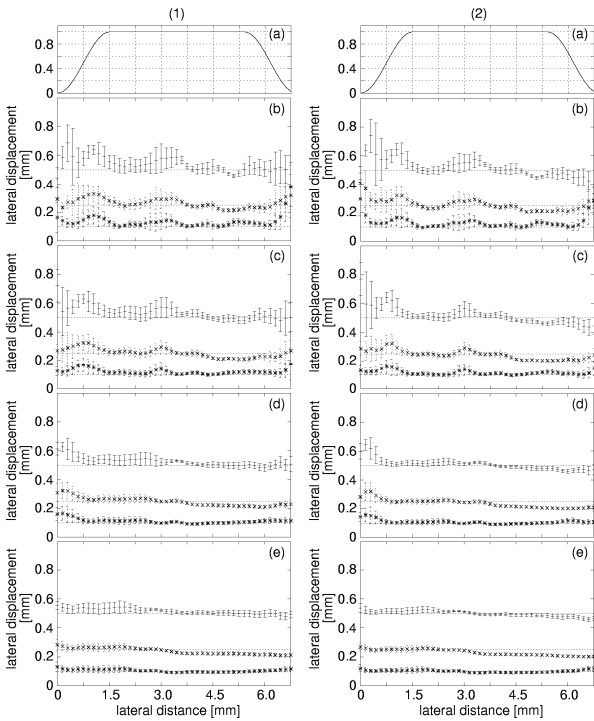


Fig. 7. Means and standard deviation of lateral displacements obtained by the estimators given by (1) Eq. (19) and (2) Eq. (25). (a) Tukey window used in the Hilbert transform. Lateral displacements estimated by the proposed method with correlation kernel sizes of (b) 0.6 mm, (c) 1.2 mm, (d) 2.4 mm, and (e) 3.6 mm. The 3 horizontal dashed lines in each figure (b)–(e) show the actual assigned displacements.

5. Conclusion

In this study, a method was developed to estimate lateral displacements using the lateral phase, which can be applied to ultrasonic echoes obtained by a conventional beamformer. In the proposed method, complex signals were generated by the Hilbert transform, and the phase shift due to the lateral

displacement was estimated by correlation-based estimators. The proposed method was validated using a cylindrical phantom mimicking an artery. As a result, the lateral displacements could be measured with an error of 13.5% of the true displacement of 0.5 mm, and the proposed method would be useful because it can be applied to ultrasonic echoes obtained by conventional beamformers.

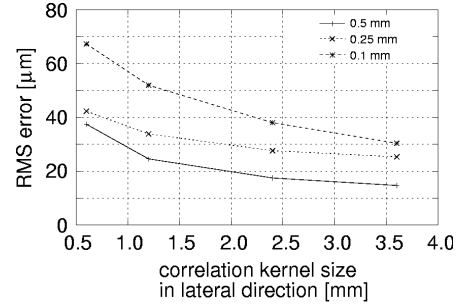


Fig. 8. Root mean square errors of lateral displacements $\{u_{x,(0,1)}(n)\}$ obtained by the proposed estimator given by (19) are plotted as a function of correlation kernel size in the lateral direction. The 3 curves show the errors in cases of actual lateral displacements of 0.1, 0.25, and 0.5 mm.

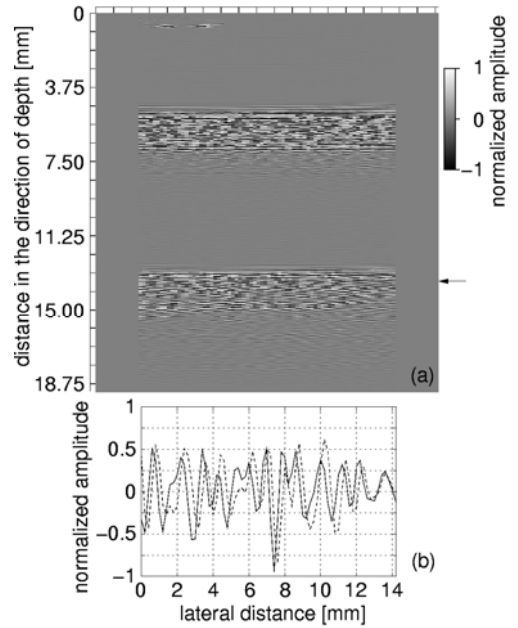


Fig. 9. Radio frequency echo from the phantom obtained by the lateral modulation method. (a) Radio frequency echo $\text{Re}\{g(x; n)\}$ obtained by in-phase receive beamforming. (b) Lateral profiles of $\{g(x; n)\}$ at a depth indicated by the arrow in (a) obtained by in-phase and quadrature receive beamforming.

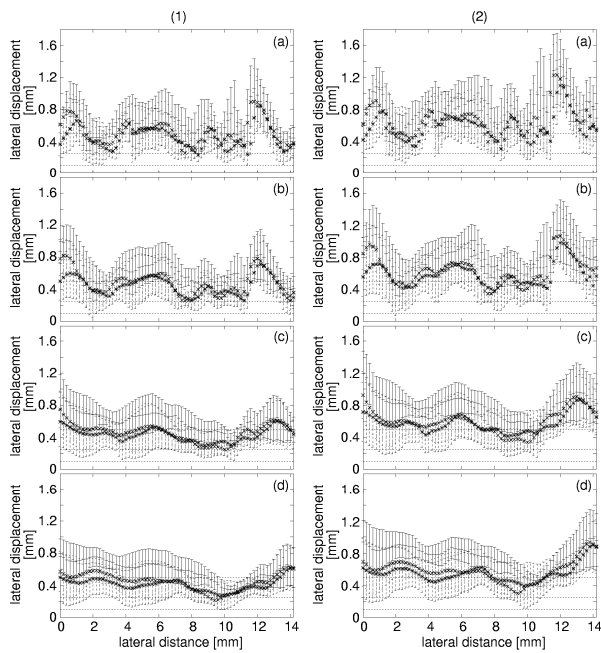


Fig. 10. Means and standard deviations of lateral displacements obtained by the lateral modulation method with (1) motion estimator given in [29] and (2) that given by (19). Means and standard deviations obtained with correlation kernel sizes of (a) 0.6 mm, (b) 1.2 mm, (c) 2.4 mm, and (d) 3.6 mm in the lateral direction. The 3 horizontal dashed lines in each figure show the actual assigned displacements.

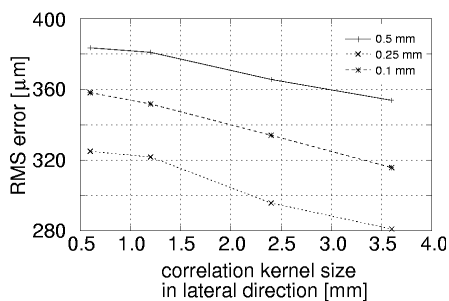


Fig. 11. Root mean square errors of lateral displacements estimated by the lateral modulation method with the motion estimator in [29] are plotted as a function of correlation kernel size in the lateral direction. The 3 curves show the errors in cases of actual lateral displacements of 0.1, 0.25, and 0.5 mm.

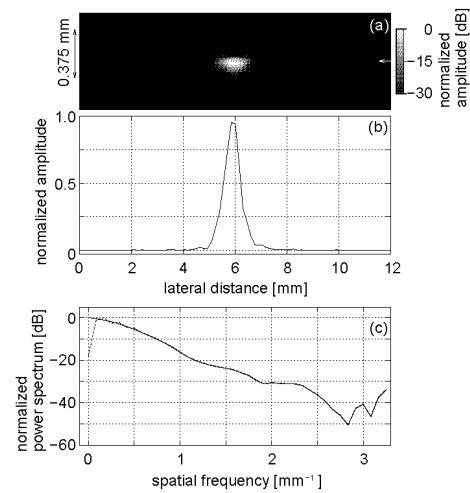


Fig. 12. (a) B-mode image of a fine wire obtained by a conventional beamformer. (b) Lateral profile of envelopes of received ultrasonic RF echoes at a depth indicated by the arrow in (a). (c) Power spectra of lateral profiles of envelopes. The solid line shows power spectrum of the envelope shown in (b). The dashed line shows power spectrum of the envelope that was obtained by removing the direct current component from (b) based on (26).

Acknowledgments

We are grateful to Panasonic Co., Ltd., and Panasonic Shikoku Co., Ltd., for providing the cylindrical phantom used in this study.

References

- [1] Lee RT, Grodzinsky AJ, Frank EH, Kamm RD and Schoen FJ. Structure-dependent dynamic mechanical behavior of fibrous caps from human atherosclerotic plaques. *Circulation* **83**, 1764–1770, 1991.
- [2] Loree HM, Grodzinsky AJ, Park SY, Gibson LJ and Lee RT. Static circumferential tangential modulus of human atherosclerotic tissue. *J Biomech* **27**, 195–204, 1994.
- [3] Simons PCG, Algra A, Bots ML, Grobbee DE and van der Graaf Y. Common carotid intima-media thickness and arterial stiffness. *Circulation* **100**, 951–957, 1999.
- [4] Falk E, Shah PK and Fuster V. Coronary plaque disruption. *Circulation* **92**, 657–671, 1995.
- [5] Davies MJ. Stability and instability: Two faces of coronary atherosclerosis. *Circulation* **94**, 2013–2020, 1996.
- [6] Golledge J, Greenhalgh RM and Davies AH. The symptomatic carotid plaque. *Stroke* **31**, 774–781, 2000.
- [7] McConnell MV, Aikawa M, Maier SE, Ganz P, Libby P and Lee RT. MRI of rabbit atherosclerosis in response to dietary cholesterol lowering. *Arterioscler Thromb and Vasc Biol* **19**, 1956–1959, 1999.
- [8] Potkin BN, Bartorelli AL, Gessert JM, Neville RF, Almagor Y, Roberts WC and Leon MB. Coronary artery imaging with intravascular high-frequency ultrasound. *Circulation* **81**, 1575–1585, 1990.

- [9] Hoeks APG, Ruisen CJ, Hick P and Reneman RS. Transcutaneous detection of relative changes in artery diameter. *Ultrasound Med Biol* **11**, 51–59, 1985.
- [10] Hoeks APG, Di X, Brands PJ and Reneman RS. Comparison of the performance of the RF cross correlation and Doppler autocorrelation technique to estimate the mean velocity of simulated ultrasound signals. *Ultrasound Med Biol* **19**, 727–740, 1993.
- [11] Länne T, Stale H, Bengtsson H, Gustafsson D, Bergqvist D, Sonesson B, Lecerof H and Dahl P. Noninvasive measurement of diameter changes in the distal abdominal aorta in man. *Ultrasound Med Biol* **18**, 451–457, 1992.
- [12] Brands PJ, Hoeks APG, Rutten MC and Reneman RS. A noninvasive method to estimate arterial impedance by means of assessment of local diameter change and the local centerline blood flow velocity using ultrasound. *Ultrasound Med Biol* **22**, 895–905, 1996.
- [13] Meinders JM, Brands PJ, Willigers JM, Kornet L and Hoeks APG. Assessment of the spatial homogeneity of artery dimension parameters with high frame rate 2-D B-mode. *Ultrasound Med Biol* **27**, 785–794, 2001.
- [14] Bergel DH. The static elastic properties of the arterial wall. *J Physiol* **156**, 445–457, 1961.
- [15] Peterson LH, Jensen RE and Parnel J. Mechanical properties of arteries *in vivo*. *Circ Res* **8**, 622–639, 1960.
- [16] Hayashi K, Handa H, Nagasawa S, Okamura A and Moritake K. Stiffness and elastic behavior of human intracranial and extracranial arteries. *J Biomech* **13**, 175–184, 1980.
- [17] Kanai H, Sato M, Koiwa Y and Chubachi N. Transcutaneous measurement and spectrum analysis of heart wall vibrations. *IEEE Trans Ultrason Ferroelect Freq Contr* **43**, 791–810, 1996.
- [18] Kanai H, Hasegawa H, Chubachi N, Koiwa Y and Tanaka M. Noninvasive evaluation of local myocardial thickening and its color-coded imaging. *IEEE Trans Ultrason Ferroelect Freq Contr* **44**, 752–768, 1997.
- [19] Hasegawa H, Kanai H, Koiwa Y and Chubachi N. Noninvasive evaluation of Poisson's ratio of arterial wall using ultrasound. *Electron Lett* **33**, 340–342, 1997.
- [20] Hasegawa H, Kanai H and Koiwa Y. Modified phased tracking method for measurement of change in thickness of arterial wall. *Jpn J Appl Phys* **41**, 3563–3571, 2002.
- [21] Kanai H, Koiwa Y and Zhang J. Real-time measurements of local myocardium motion and arterial wall thickening. *IEEE Trans Ultrason Ferroelect Freq Contr* **46**, 1229–1241, 1999.
- [22] Kanai H, Hasegawa H, Ichiki M, Tezuka F and Koiwa Y. Elasticity imaging of atheroma with transcutaneous ultrasound -preliminary study-. *Circulation* **107**, 3018–3021, 2003.
- [23] Cinthio M, Ahlgren AR, Jansson T, Eriksson A, Persson HW and Lindström K. Evaluation of an ultrasonic echo-tracking method for measurements of arterial wall movements in two dimensions. *IEEE Trans Ultrason Ferroelect Freq Contr* **52**, 1300–1311, 2005.
- [24] Ribbers H, Holewijn S, Blankensteijn JD, and de Korte CL. Non-invasive two dimensional elastography of the carotid artery. *Proc 2005 IEEE Ultrason Symp*, 1113–1116, 2005.
- [25] Ophir J, Céspedes I, Ponnekanti H, Yazdi Y and Li X. Elastography: A quantitative method for imaging the elasticity of biological tissues. *Ultrason Imaging* **13**, 111–134, 1991.
- [26] Céspedes I and Ophir J. Reduction of image noise in elastography. *Ultrason Imaging* **15**, 89–102, 1993.
- [27] Konofagou EE, Ophir J, Varghese T and Kallel F. A new elastographic method for estimation and imaging of lateral displacements, lateral strains, corrected axial strain and Poisson's ratios in tissues. *Ultrasound Med Biol* **24**, 1183–1199, 1998.
- [28] Ophir J, Garra B, Kallel F, Konofagou E, Krouskop T, Righetti R, and Varghese T. Elastographic imaging. *Ultrasound Med Biol* **26**, S23–S29, 2000.
- [29] Jensen JA and Munk P. A new method for estimation of velocity vectors. *IEEE Trans Ultrason Ferroelect Freq Contr* **45**, 837–851, 1998.
- [30] Chen X, Zohdy MJ, Emelianov SY and O'Donnell M. Lateral speckle tracking using synthetic lateral phase. *IEEE Trans Ultrason Ferroelectr Freq Contr* **51**, 540–550, 2004.
- [31] Hasegawa H and Kanai H. Phase-sensitive lateral motion estimator for measurement of artery-wall displacement – phantom study. *IEEE Trans Ultrason Ferroelect Freq Contr* **56**, 2450–2462, 2009.
- [32] Hasegawa H and Kanai H. Reduction of influence of variation in center frequencies of RF echoes on estimation of artery-wall strain. *IEEE Trans Ultrason Ferroelect Freq Contr* **55**, 1921–1934, 2008.
- [33] Kasai C, Namekawa K, Koyano A and Omoto R. Real-time twodimensional blood flow imaging using an autocorrelation technique. *IEEE Trans Son Ultrason SU-32*, 458–464, 1985.
- [34] Hasegawa H and Kanai H. Simultaneous imaging of artery-wall strain and blood flow by high frame rate acquisition of RF signals. *IEEE Trans Ultrason Ferroelect Freq Contr* **55**, 2626–2639, 2008.
- [35] Kanai H, Sato M, Koiwa Y and Chubachi N. Transcutaneous measurement and spectrum analysis of heart wall vibrations. *IEEE Trans Ultrason Ferroelect Freq Contr* **43**, 791–810, 1996.